30.0 MECHANISMS OF GRAIN REFINEMENT IN LASER POWDER BED FUSION OF IN-SITU METAL MATRIX COMPOSITE 6061 ALUMINUM ALLOYS

Chloe Johnson (Mines)
Faculty: Amy Clarke (Mines)
Industrial Mentors: Paul Wilson (Boeing), John Carpenter (LANL), and Jeremy Iten (Elementum 3D)

This project was initiated in Fall 2017 and is supported by the George S. Ansell Department of Metallurgical and Materials Engineering Fellowship, A.J. Clarke's startup funds at the Colorado School of Mines (Mines), CANFSA, and the National Science Foundation (NSF). The research performed during this project will serve as the basis for a Ph.D. thesis for Chloe Johnson.

30.1 Project Overview and Industrial Relevance

Additive manufacturing (AM) allows for the design and production of near net shape components, as well as the incorporation of complex internal networks (*e.g.* cooling channels or lattices) inside of parts by 3D printing. Despite these advantages, the number of printable alloys is currently limited due to the far from equilibrium solidification conditions experienced during AM. This is especially seen in Al alloys, where a large thermal conductivity and low laser absorptivity contribute to a higher thermal gradient (G) and a necessity for higher laser powers, respectively. Additionally, the large solidification ranges of these alloys can lead to solidification cracking, which occurs in the final stages of solidification, where solute-rich liquid in between grains shrinks with no excess liquid to backfill this region [30.1]. A few strategies have been suggested to address these issues, primarily focusing on grain refinement via alloying and/or inoculation, or by controlling solidification conditions via process parameters to induce a columnar to equiaxed transition (CET). While some success has been achieved by alloying or optimizing laser parameters, the former limits the number of alloys that can be used, while the latter does not translate across material systems and equipment [30.1]. Refinement via inoculation has been shown to produce a refined, equiaxed microstructure free of solidification cracking that achieves good mechanical properties [30.2]. However, studies on inoculated Al alloys are limited, and mostly focus on proof of concept, rather than identifying specific grain refinement mechanisms. This study proposes to investigate grain refinement mechanisms in inoculated A6061-RAM (reactive additive manufacturing) alloys developed and designed for AM by Elementum 3D. These alloys contain micron-scale additive powders that dissolve in the melt, undergo a thermodynamically favorable reaction, and form submicron-scale particles that serve as inoculants to refine the microstructure (**Figure 30.1)**. Additionally, some of the additive reactant powders do not fully dissolve during processing. In combination with finer, inoculant product particles, they serve to effectively create a metal matrix composite (MMC) with improved mechanical performance. *In-situ* and ex-situ microstructural characterization techniques will be used to understand grain refinement mechanisms in A6061-RAM alloys, which will add to the variety of inoculated Al alloys for potential use in AM, as well as help to inform fundamental understanding of grain refinement mechanisms in these alloys.

30.2 Previous Work

In-situ imaging of the solidification of 1 mm long laser rasters performed at the Advanced Photon Source (APS) at Argonne National Laboratory (ANL) was analyzed to consider how solidification conditions impact grain refinement in A6061-RAM alloys compared to traditional, wrought 6061. Solidification velocity and thermal gradient were considered for this study, the former measured from the images captured in these experiments and the latter estimated using Rosenthal modeling. These results were then compared to the observed microstructures in the melt pools. Based on these results, it was found that A6061-RAM2 (the 2 referring to the vol. % of Ti and B_4C added to the initial powder feed stock in a ratio of 3:1) fully refined the microstructure to ~2 μm for all laser conditions studied.

Additionally, an initial look at the structures of AM builds produced using different starting RAM contents (0.5, 1, 2, and 10 vol. %) was performed. Electron back scatter diffraction (EBSD) inverse pole figure (IPF) maps showed an increase in refinement as RAM content increased, with little additional refinement being observed above the 2 vol. % amount (**Figure 30.2**). Corresponding SEM images and energy dispersive spectroscopy (EDS) results indicated that in alloys containing both columnar and equiaxed growth regions (i.e. 0.5 and 1 vol. %), the former region did not contain particles, while the latter contained Ti-rich particles.

A heat treatment study performed on A6061-RAM2, A6061-RAM10, and 6061 wrought and AM built samples gave an overview of heat treatment response in these alloys for aging parameters based on the standard T6 treatment for 6061. Material properties were evaluated using Vickers microhardness and changes in microstructure were observed using SEM. A6061-RAM2 was found to achieve similar, if not slightly higher, hardness values than 6061 wrought, with A6061-RAM10 showing even higher hardness values. Unexpectedly, coarse precipitates (i.e. able to be seen using SEM imaging, or at least a few hundred microns in size) were also observed in the RAM alloys, and it was proposed that these phases nucleated off of existing particles from the RAM process in the as-solidified microstructure in these alloys, leading to a premature coarsening.

30.3 Recent Progress

The final component of this project is focused on identifying the formation of various particles in A6061-RAM alloy microstructures and how they contribute to refinement in these alloys. AM builds isolating each component of the A6061-RAM2 alloy were performed to consider their contribution to refinement, and compared to the structure of the alloy containing both components (i.e. Ti and B_4C). These will be referred to as A6061-RAM(Ti) and A6061-RAM(B_4C), which each contain the same amount of their additive as that contained in the A6061-RAM2 for direct comparison. Additionally, a RAM alloy consisting of a commercially pure Al matrix with the same amount of Ti added as the A6061-RAM(Ti) and A6061-RAM2 was also considered to isolate the role of solute in refinement of these alloys. While this study will also consider the impact of increasing RAM content (i.e. increasing the vol. % added of both Ti and B_4C to the base alloy powder in a ratio of 3:1), more focus will be given to the previously mentioned alloys in this report. An overview of the grain structure shows refinement throughout the structure for A6061-RAM2 and A6061-RAM(Ti) alloys, with regions of refinement and columnar growth observed in A6061-RAM(B_4C) and Al-Ti (**Figure 30.3**). Previous reports focusing on SEM investigation found Ti-rich particles located in regions of refinement in all alloys except for A6061-RAM(B_4C), where particles were difficult to observe in the SEM, either due to size or contrast comparted to the matrix.

30.3.1 Solute Distribution

The in-situ nature of the RAM process implies a need to understand solute distribution in these alloys, specifically investigating the dissolution and distribution of the initial reacting particles. To gain insight into Ti solute distribution, as well as the impact of additional solute from both 6061 alloying elements and B_4C, electron microprobe mapping was performed on both as built Al-Ti and A6061-RAM2. These maps (**Figure 30.4**) show the relative distribution of Ti in both alloys is somewhat inhomogeneous, and is most likely based on where the convection and turbulence from the laser melting process move solute within the melt. It also appears that the additional solutes in the A6061-RAM2 alloy do not have a significant impact on the distribution of Ti. However, Si was also found to be inhomogenously distributed, with preference to segregate to areas with more Ti. This has been observed during aging of these alloys both in previous work for this project and in literature [30.3], and was proposed in the previous heat treatment study to have aided nucleation of Mg-Si precipitates on Ti-rich particles.

30.3.2 Observed Particles and Phases

Previous reports focusing on SEM investigation found Ti-rich particles located in regions of refinement with no particles being observed in regions of columnar growth. Phase identification of these particles, as well as their location within the microstructure, could be indicative of which phases contribute to grain refinement. This investigation began with X-ray diffraction (XRD) (**Figure 30.5**). Due to the small volume fraction of each particle type, an experiment to dissolve the aluminum matrix was performed to improve detection of these phases. The results of this for A6061-RAM2 showed improved detection of peaks other than the aluminum matrix (**Figure 30.5**), and is currently being performed on additional RAM alloys to further the understanding of phases. These results show the presence of Al_3Ti in the stable $D0_{22}$ form, with no detection of the Al_3Ti $L1_2$ phase that has been reported as an inoculant in Al-Ti rapid solidification literature [30.4, 30.5]. It also shows the presence of TiB_2 and AlB_2, as well as the strengthening phase for 6061 alloys, Mg_2Si.

To correlate particle type to microstructural location, as well as investigate any phases existing in a small enough phase fraction as to not be detected by XRD, transmission electron microscopy (TEM) and EDS through scanning TEM (STEM) was performed. While more work remains to be done on additional alloys, Al-Ti and A6061-

RAM(Ti) particles have been explored. A summary of the observed particle types, morphology, chemistry, and location, as well as example images, for each of these alloys reveals similar results (**Table 30.1 & Figure 30.6**). The two particles seen to form inside of grains, and thus those most likely to contribute to grain refinement, are the petal/cubic or rectangular/blocky particles. The Al-Ti phase diagram (**Figure 30.7**) suggests these Al and Ti containing phases to be the Al_3Ti peritectic phase, and based on XRD, are most likely the Al_3Ti $D0_{22}$ structure. TEM electron diffraction is currently being done to explore this further. Upon closer observation, these particles were also seen to have a dendritic/cellular morphology (**Figure 30.6c&f**), which has been attributed to the growth velocity being slower than the critical velocity needed to maintain a planar interface [30.5].

30.3.3 Potential Refinement Mechanisms

Refined regions in all RAM alloys investigated appear to correspond to where particles have formed. Because of this, it is important to consider what allows or restricts particles from forming, as well as which particles may/may not contribute to refinement. For the two alloys considered in detail for this reporting period, namely Al-Ti and A6061-RAM (Ti), particles observed in the centers of grains are either of a cubic/petal or a rectangular morphology, containing both Al and Ti, and most likely correspond to the peritectic Al_3Ti phase based on the Al-Ti phase diagram. While in the A6061-RAM(Ti) refinement is seen throughout the melt pool, in the Al-Ti there are various regions of refinement based on where these particles form. To identify which location in the melt these particles form, and any possible dependence of their formation on local solute or solidification conditions, a sample of this alloy was etched in Kroll's reagent (**Figure 30.8**). The etched sample shows that while refinement is observed in the bottom of most melt pools, it is also observed in random regions of the melt pools as well. This is also evidenced in the microprobe maps of Al-Ti (**Figure 30.4**), in which Ti rich regions appear to be slightly less homogenous, or have a localized higher intensity of counts in certain regions of the melt. This evidence suggests that the location of particle formation is most likely not dependent on solidification conditions, so much as where the particles happened to be pushed in the melt due to contributions like convection or turbulence. This was also observed in the A6061-RAM(B_4C) sample upon etching (**Figure 30.8b**), suggesting that this alloy experiences a similar phenomenon.

30.4 Plans for Next Reporting Period

The plans for next reporting period include:

- Investigation of phases/particles in remaining alloys;
- Thesis writing and completion.

30.5 References

[30.1] J. Zhang, B. Song, Q. Wei, D. Bourell, Y. Shi, A Review of SLM of Aluminum Alloys: Processing, Microstructure, Property, and Developing Trends, Journal of Materials Science and Technology. 35 (2019) 270-284.

[30.2] J. H. Martin, B. D. Yahata, J. M. Hundley, J. A. Mayer, T. A. Schaedler, T. M. Pollock, 3-D Printing of High-Strength Aluminium Alloys, Nature. 549 (2017) 303-314.

[30.3] E. M. Sullivan, Influence of Reaction Synthesis Feedstocks on Solidification Defect Formation and Microstructure-Property Relationships in Electron Beam Freeform Fabrication of Aluminum Metal Matrix Composites, Colorado School of Mines. (2021).

[30.4] Q. Tan, J. Zhang, Q. Sun, Z. Fan, G. Li, Y. Yin, Y. Liu, M. X. Zhang, Inoculation Treatment of an Additively Manufactured 2024 Aluminium Alloy with Titanium Nanoparticles, Acta Materialia. 196 (2020) 1-16.

[30.5] M.G. Chu, Microstructure and Solidification Analysis of Melt-Spun Al-Ti and Al-Ti-B Alloys, Materials Science and Engineering. A179/A180 (1994) 669-675.

30.6 Figures and Tables

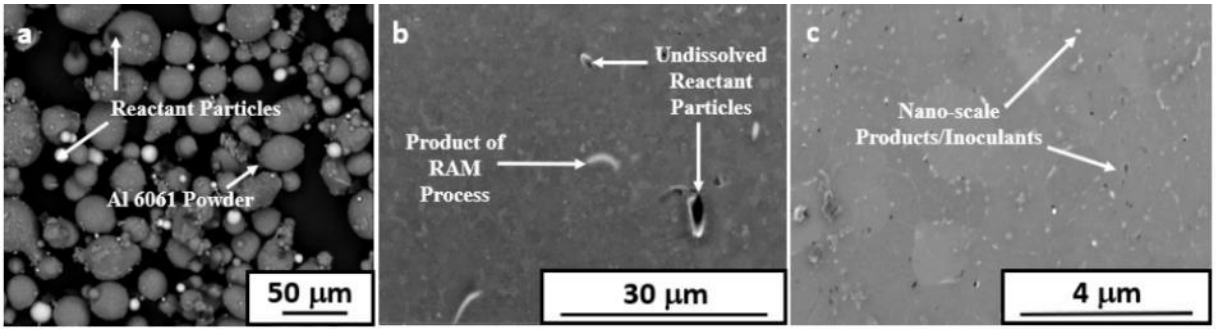

Figure 30.1: Backscattered electron SEM images of a) the 6061 RAM with 2% inoculant powder feedstock and b) the general microstructure of an as-built cube after the laser powder bed fusion build process. The arrows show initial and unreacted inoculant powders before and after the build process. c) A secondary electron SEM image of the submicron-size products/inoculants from the RAM process, which can be seen in and around the grains.

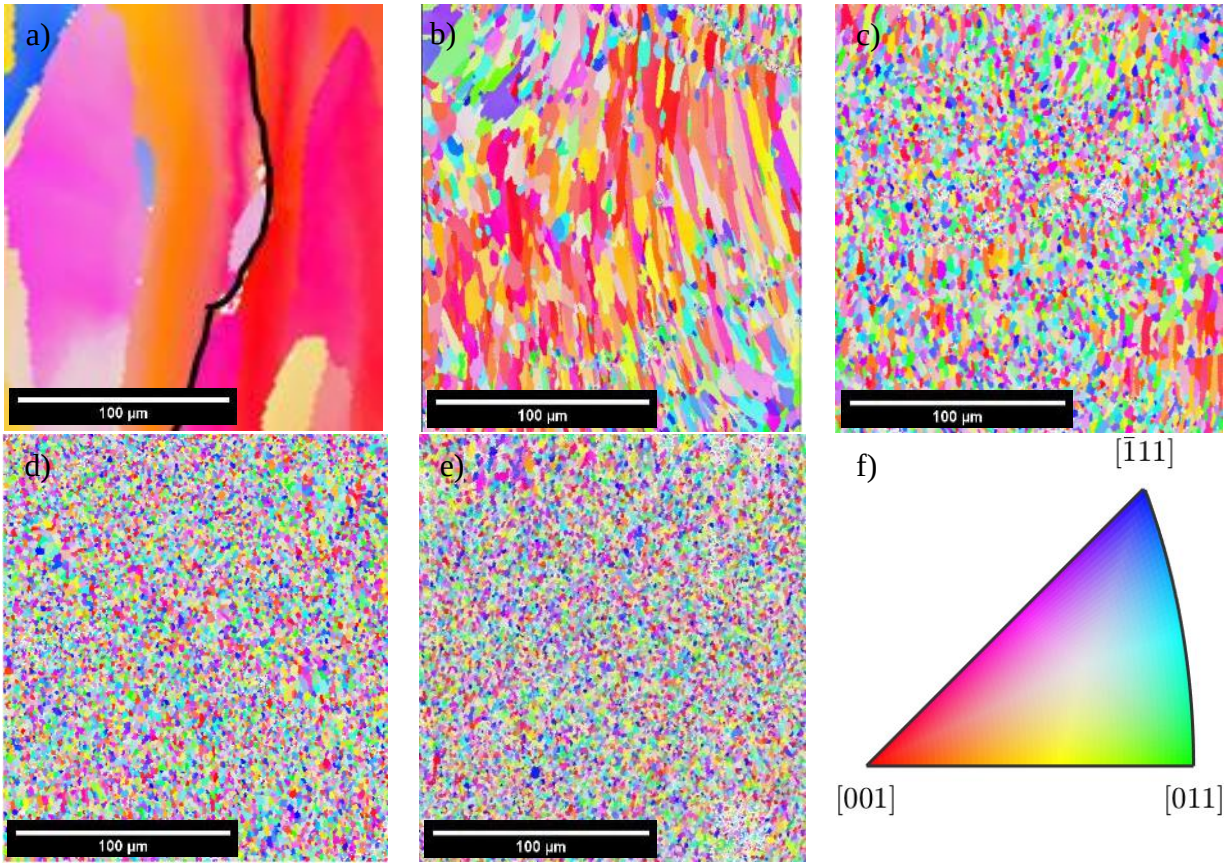

Figure 30.2: EBSD IPF maps for samples containing various starting reactive particle contents: a) 6061 (no RAM particles), b) RAM0.5, c) RAM1, d) RAM2 and d) RAM10. Each number represents the vol % of RAM added with a ratio of 3:1 Ti:B_4C. The standard triangle is given in f), the build direction is upwards for all images, and the EBSD IPF maps are colorized parallel to the build direction.

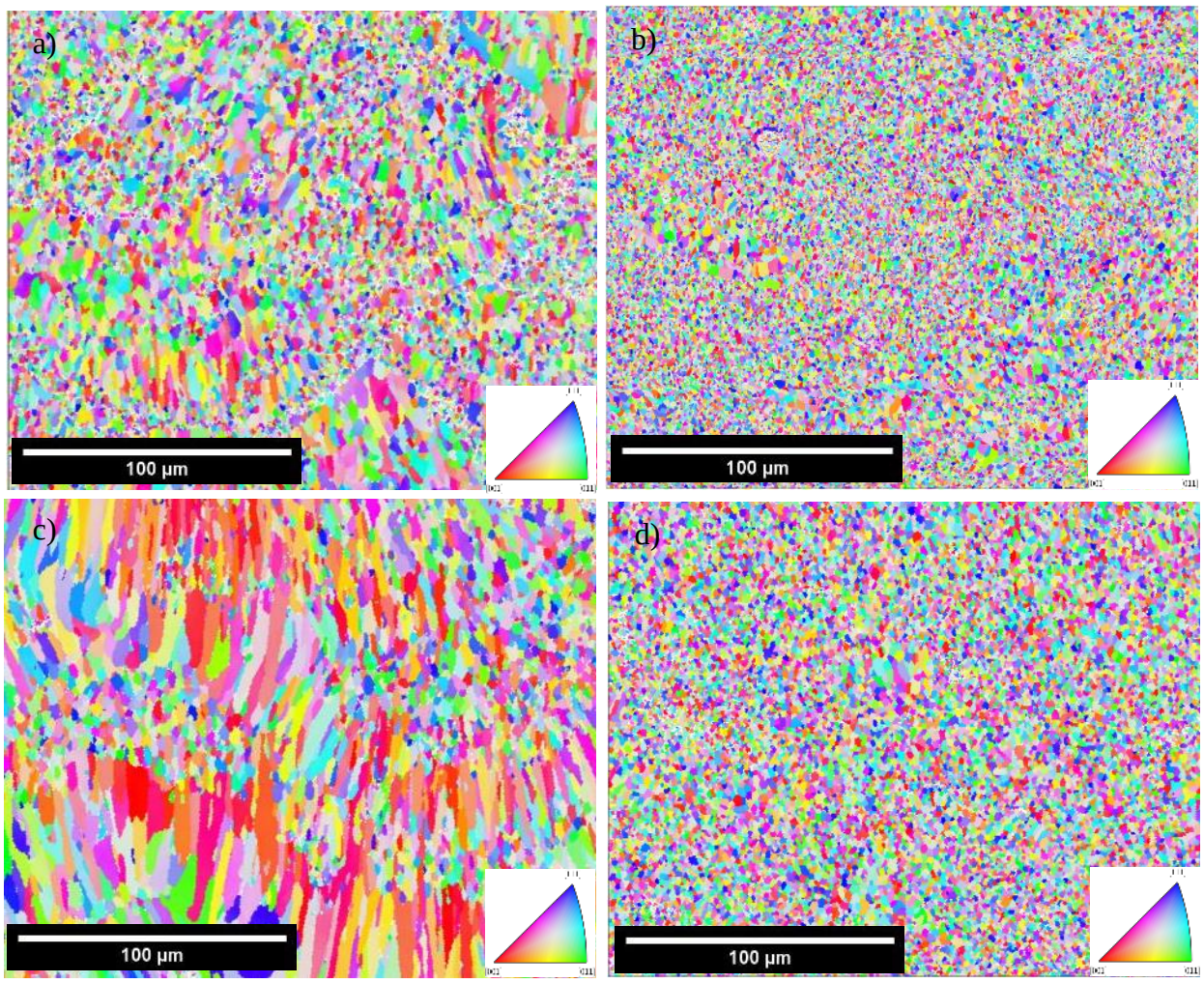

Figure 30.3: EBSD inverse pole figure (IPF) maps, showing the grain structure of a) Al-Ti, b) A6061-RAM(Ti), c) A6061-RAM(B_4C), and d) A6061-RAM2.

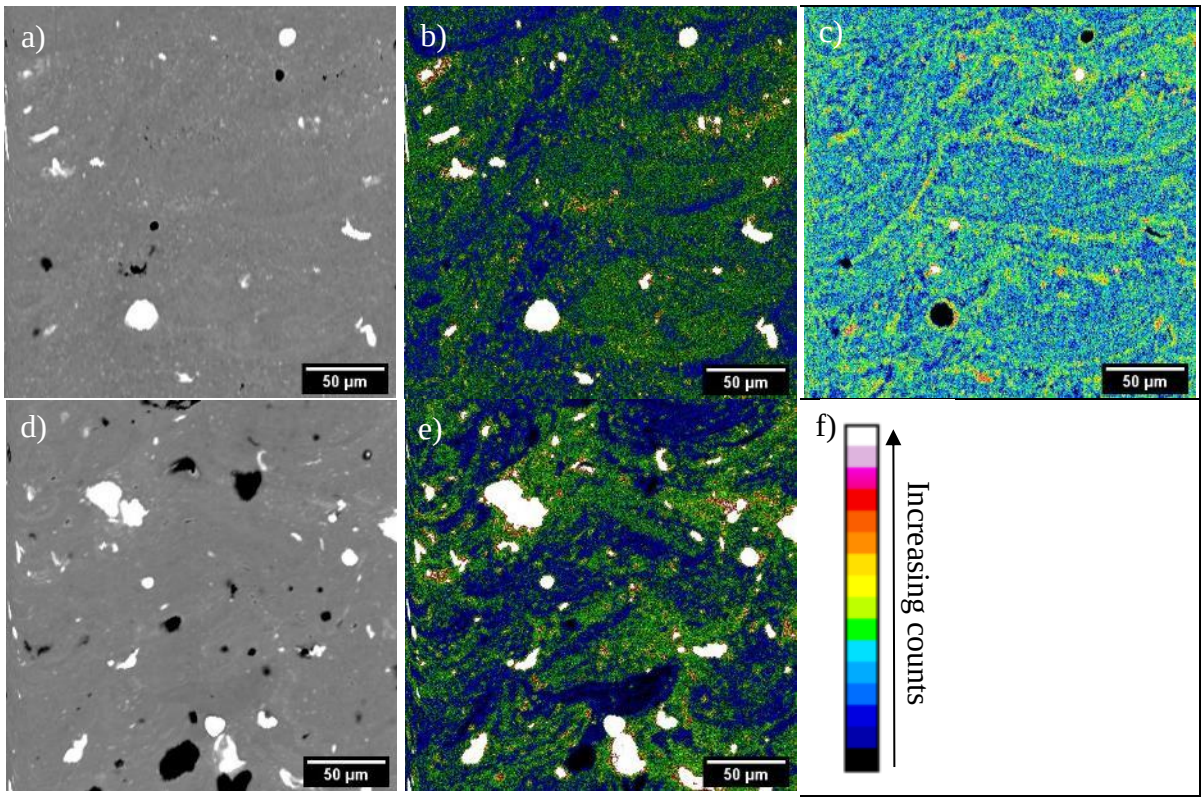

Figure 30.4: Electron microprobe results, showing solute distribution in a)-c) A6061-RAM2 and d)-e) Al-Ti with the same amount of added Ti. a) and d) are SEM back-scatter images of the region in the build, b) and e) show the Ti solute distribution, and c) shows the Si in the A6061-RAM2. The build direction is upwards, and the images are colorized based on a grey scale value that correlates to counts from the original greyscale data. A relative scale is shown in f). White particles in the SEM images correspond to Ti particles, while black particles are either B_4C or porosity in the sample.

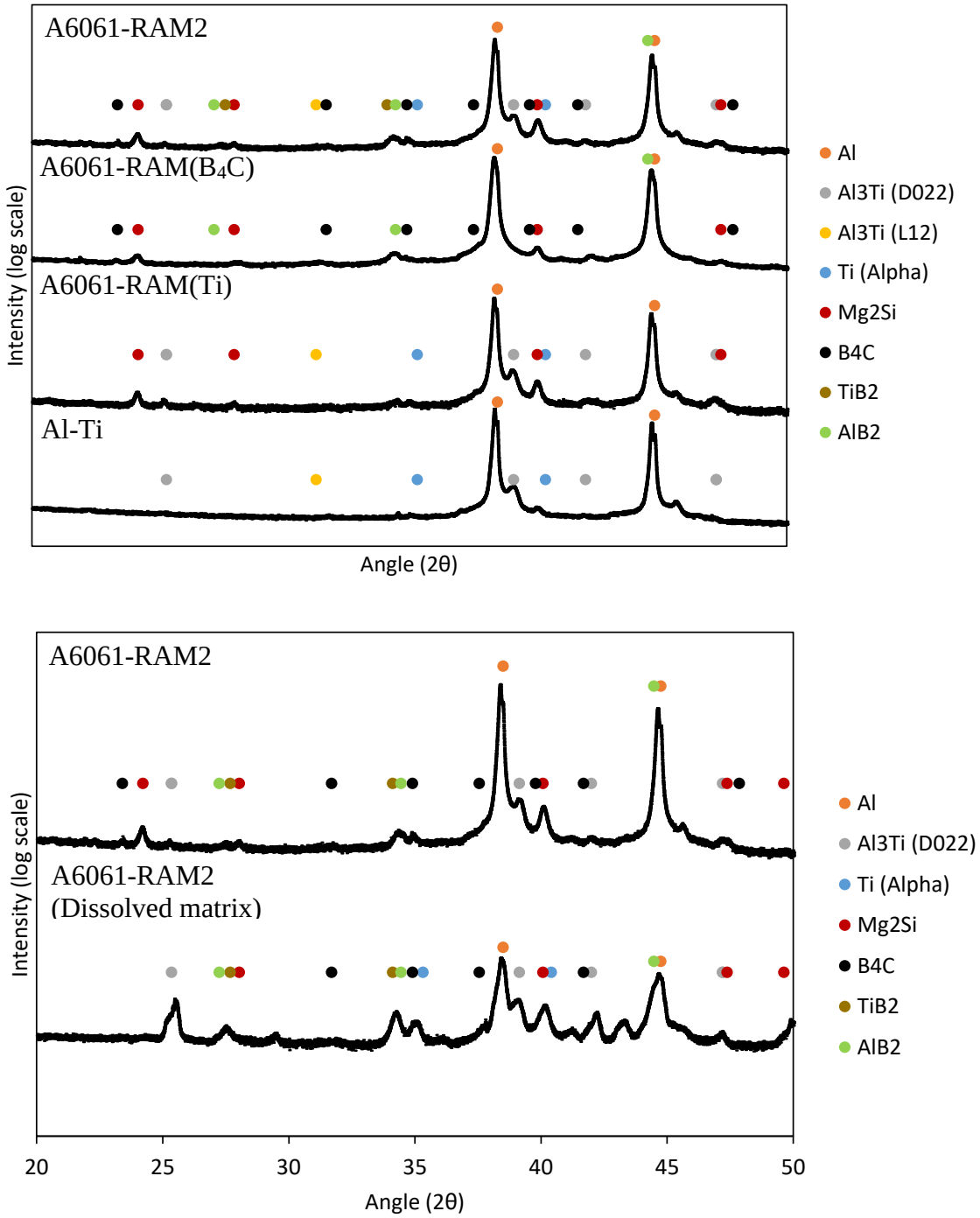

Figure 30.5: X-ray diffraction (XRD) results for various RAM alloys (top) and comparison of results for A6061-RAM2 and the same alloy following dissolution of the alloy matrix (bottom).The 20-50° range for 2θ was chosen based on where higher intensity values were observed for simulations of these particles. A Cu source was used for XRD.

Table 30.1: Characteristics of particles observed in selected RAM alloys.

Alloy	Morphology	Size (nm)	Chemistry (wt. %)	Location
Al-Ti	Petal/cubic	140 ± 110	Al: 80.6 ± 6.7 Ti: 18.4 ± 5.7 Al/Ti = 4.8 ± 1.7	center of grains, other regions of grains/over boundaries
	Rectangular/blocky	310 ± 90 x 150 ± 40	Al: 75.1 ± 4.0 Ti: 20.5 ± 4.6 Al/Ti = 3.9 ± 1.2	center of grains, other regions of grains/over boundaries
	Fine	<30	Al: 91.2 ± 1.1 Ti: 8.4 ± 1.1 Al/Ti: 11.1 ± 1.7	dispersed throughout matrix
A6061-RAM(Ti)	Petal/cubic	180 ± 120	Al: 75.66 ± 5.06 Ti: 21.62 ± 4.82 Si: 0.32 ± 0.25 Cu: 1.90 ± 0.61 Al/Ti = 3.76 ± 1.25	center of grains, other regions of grains/over boundaries
	Rectangular/blocky	320 ± 110 x 320 ± 30	Al: 70.72 ± 5.47 Ti: 25.14 ± 5.74 Si: 1.20 ± 0.51 Cu: 1.91 ± 0.66 Al/Ti = 2.97 ± 0.82	center of grains, other regions of grains/over boundaries
	Fine	<30	Al: 86.67 ± 5.06 Ti: 10.30 ± 3.75 Si: 0.63 ± 0.98 Cu: 1.81 ± 0.32 Al/Ti: 9.62 ± 4.09	dispersed throughout matrix

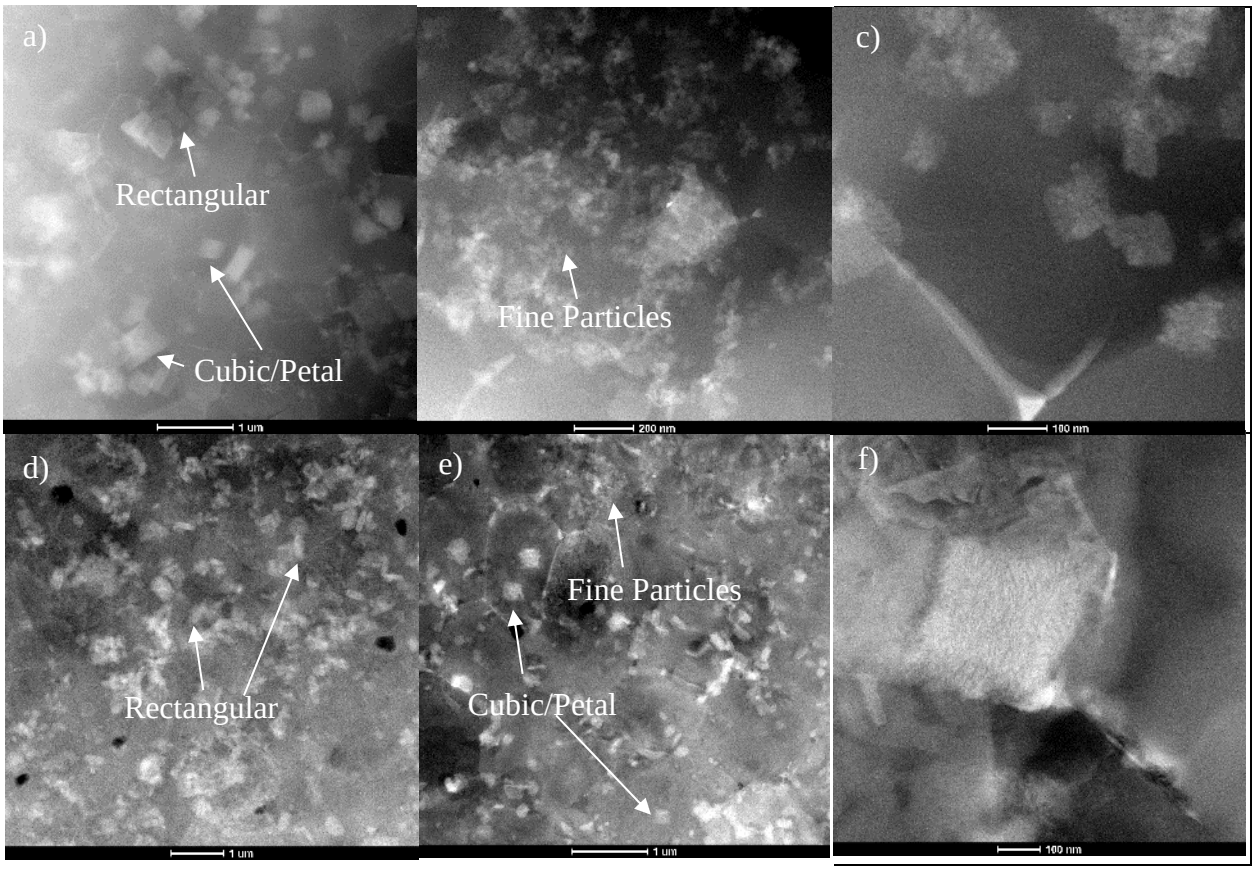

Figure 30.6: STEM images of Ti-rich particles observed in a)-c) Al-Ti and d)-f) A6061-RAM(Ti). c) and f) specifically highlight the non-planar structure of the cubic/petal particles.

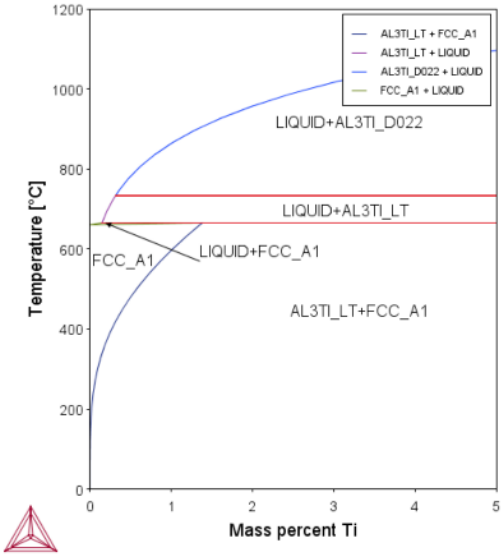

Figure 30.7: Al-Ti phase diagram simulated in Thermo-Calc software, where FCC_A1 is alpha aluminum and AL3TI_LT is a low temperature tetragonal phase of Al_3Ti, similar to the $D0_{22}$ structure.

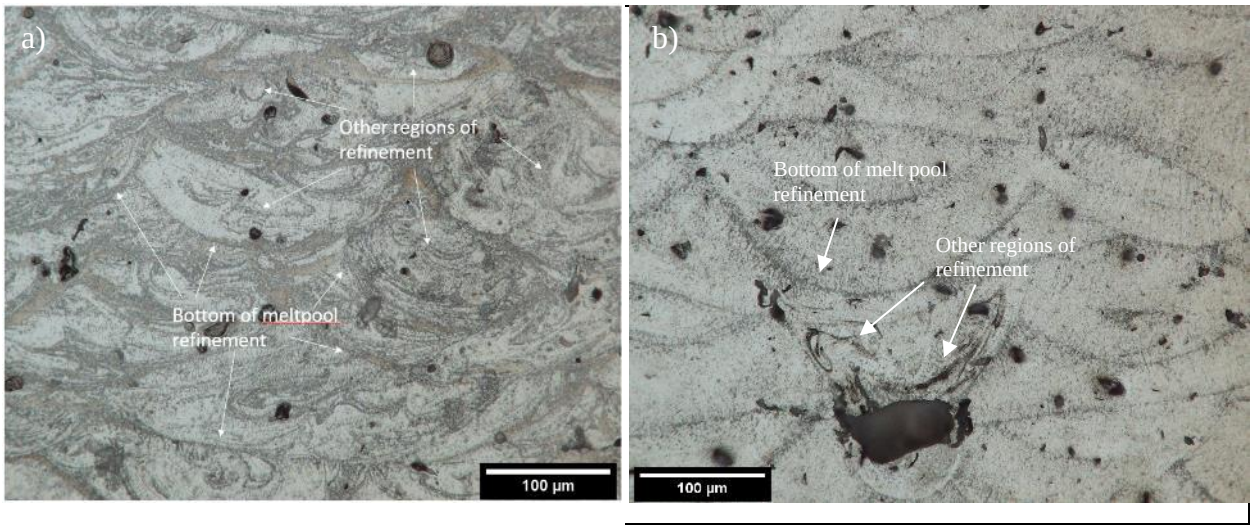

Figure 30.8: Light optical images of AM builds of a) A6061-RAM(Ti) and b) A6061-RAM(B_4C), etched using Kroll's reagent.